RSC Advances

PAPER

View Article Online
View Journal | View Issue

Cite this: *RSC Adv.*, 2025, **15**, 14235

Directed hydrogenolysis of "cellulose-to-ethylene glycol" using a Ni–WO_x based catalyst†

Tong Su, Daguo Wu, Xinghua Zhang, Qi Zhang, Lungang Chen, Xiuzheng Zhuang* and Longlong Ma

Biomass is an important renewable resource in nature, and cellulose is a crucial component within it. The chemically directed conversion of cellulose into ethylene glycol offers a green alternative to traditional petroleum-based production methods. In this study, a multifunctional Ni–WO_x/SAPO-11 catalyst was designed. By optimizing the processing parameters of catalysts and the reaction conditions of them, it was demonstrated that this catalyst could efficiently catalyze cellulose into alcohol products through a series of tandem reactions such as hydrolysis, retro-aldol condensation, and hydrogenation under relatively mild conditions. The yield of ethylene glycol climbed from 4% (at 180 °C) to 66.6% (at 240 °C) with the increase of reaction temperature. Characterization (XPS, TEM, TPD/TPR) revealed that a reduction temperature of 500 °C maximized Brønsted acidity and W^{5+}/W^{6+} ratios, enhancing C–C cleavage efficiency. Further increases in the reduction temperature would weaken the Brønsted acid on the surface of SAPO-11, but its surface area would also increase (mainly in the form of mesopores). The uniformly dispersed elemental tungsten could form new acidic sites on the catalyst surface; in combination with active Ni^0, this high-temperature reduced catalyst could achieve the direct hydrogenolysis of cellulose to produce ethylene glycol, benefiting the efficient utilization of lignocellulosic biomass in the future.

Received 4th March 2025
Accepted 21st April 2025

DOI: 10.1039/d5ra01528f

rsc.li/rsc-advances

1. Introduction

With the continuous growth of global energy demands and the urgent pursuit of environmental sustainability, developing renewable resources for producing high-value chemicals has become imperative. As the most abundant biomass resource on Earth, cellulose has emerged as a sustainable alternative to fossil fuels, garnering significant research attention.[1–3] Currently, cellulose can be catalytically converted through chemical methods into low-carbon alcohol chemicals such as 1,2-propanediol (1,2-PG), ethylene glycol (EG), and ethanol, which hold significant market economic value. Among these, EG has well-established applications across various fields; it can be used to synthesize polyester fibers and films, as well as serve in industrial applications such as antifreeze agents, coolants, and desiccants. Conventional ethylene production routes relying on petroleum or natural gas suffer from high energy intensity and poor atom economy, limiting their competitiveness. Therefore, developing a method to directly and efficiently convert renewable cellulose into low-carbon alcohols like ethylene glycol is of great significance.

In recent years, Zhang *et al.*[4] reported the direct hydrogenolysis of cellulose into EG using a Ni–W_2C/AC catalyst, achieving a breakthrough in one-step chemical catalytic conversion of cellulose to C_2 molecular alcohols. Cellulose primarily consists of glucose units linked by specific chemical bonds,[5] its highly crystalline ordered structure and strong intra/intermolecular hydrogen bonding energies make cellulose difficult to dissolve in conventional solvents and challenging to hydrolyze efficiently under mild conditions.[6,7] The reaction pathway for converting cellulose to low-carbon alcohols like ethylene glycol is also intricate: glucose and fructose can not only undergo direct hydrogenation but may also undergo C–C bond cleavage to generate various low-carbon intermediates. This process requires balancing C–C cleavage activity (for glucose) and hydrogenation capacity (for glycolaldehyde intermediates) to enhance their synergistic efficiency in promoting EG formation. These factors collectively lead to high energy consumption, numerous side reactions, and poor selectivity during conversion process. In addition, while ensuring the efficiency of the catalyst, its stability also needs to be taken into consideration. This highlights the necessity to design catalysts capable of guiding reaction pathways in appropriate sequences, as well as exploring scalable catalyst preparation processes and optimized structure–activity relationships to improve the catalytic efficiency of the "cellulose-to-ethylene glycol" process.

In previous studies, tungsten (W) and its derivatives have been demonstrated to effectively facilitate C–C bond cleavage

Key Laboratory of Energy Thermal Conversion and Control of Ministry of Education, School of Energy and Environment, Southeast University, Nanjing 210096, People's Republic of China. E-mail: zhuangxz@seu.edu.cn

† Electronic supplementary information (ESI) available. See DOI: https://doi.org/10.1039/d5ra01528f

during the hydrolysis of cellulose into small-molecule sugar alcohols. These species can synergize with highly active hydrogenation metal sites, thereby enhancing ethylene glycol (EG) yield.

Building on this foundation, Xin *et al.*[8] developed a Pd@WO_x–$MSiO_2$ YSNSs catalyst, achieving 99.3% glucose conversion and 59.4% EG selectivity. Its unique yolk–shell structure ensures higher stability, but its acidity may not be sufficient to hydrolyze cellulose. Weng *et al.*[9] employed Ru as active sites to investigate the combined effects of pore sizes in supports on catalytic activity for cellulose hydrogenolysis, attaining 51.5% EG yield. Similarly, Huang *et al.*[10] prepared Ru–WO_x/biochar *via in situ* reduction of biochar, achieving 68.8% EG yield with lower energy consumption. However, the high cost of precious metals like Pd and Ru has shifted research focus toward more cost-effective alkaline earth metals. Nickel, in particular, exhibits strong hydrogenation activity at larger particle sizes (>10 nm)[11–13] and shows further improved performance when combined with tungsten to form bifunctional catalysts. For instance, Li *et al.*[14] synthesized a Ni–W/M catalyst, where the formation of Ti–O–W bonds endowed excellent stability and 68.7% EG yield. However, the synthesis process was complex. Yang *et al.*[12] prepared a $NiCu/WO_3$ catalyst, where dual-metal sites enhanced selectivity toward diol products, achieving 83.9% total diol selectivity (58.9% for EG). Nevertheless, despite the improved low-carbon alcohol yields achieved through W-containing systems with alkaline earth metals (*e.g.*, Ni), the synergistic relationships between these components remain poorly understood. Most studies focus on empirical metal screening rather than systematic investigation of metal–support structure–activity correlations, resulting in persistent conversion bottlenecks in the "cellulose-to-ethylene glycol" process.

In this work, SAPO-11 was selected as the catalyst support. SAPO-11 is commonly employed in alkane hydroisomerization,[15] its application in hydrogenolysis reactions remains underexplored. Its unique one-dimensional pore structure, moderate aperture size, and relatively mild acidity compared to other molecular sieves make it advantageous for property modulation to control product selectivity. We prepared a series of Ni–WO_x/SAPO-11 catalysts for the "cellulose-to-ethylene glycol" conversion process. By optimizing metal ratios and reduction temperatures, near-complete cellulose conversion was achieved with 75.5% selectivity toward low-carbon alcohols, of which 66.6% was ethylene glycol. Comprehensive characterizations were conducted to investigate the catalyst morphology, physical properties, and acidity effects on EG conversion efficiency. A synergistic Ni–W catalytic reaction pathway and mechanism were proposed, providing theoretical insights for the efficient utilization of lignocellulosic biomass.

2. Experimental section

2.1 Chemicals and materials

The SAPO-11 support was procured from the Nankai University Catalyst Plant. Microcrystalline cellulose (CAS: 9004-34-6) was obtained from Merck Biochemical Technology Co., Ltd. Other chemicals, including ethylene glycol (AR, 98%), 1,2-propanediol (99%), D-sorbitol (99.5%), ammonium tungstate (99.95% metals basis), ammonium metatungstate (99.5% metals basis), nickel chloride (99%), and chloroplatinic acid (AR, Pt ≥37.5%), were also sourced from Merck Biochemical Technology Co., Ltd. D-Glucose (AR, 99%), D-fructose (AR, 99%), *n*-propanol (AR, 99%), methanol (AR, 99%), erythritol (AR, 99%), and nickel nitrate (≥98%) were purchased from Aladdin Reagent Co., Ltd. Ethanol (AR, 99.7%) was acquired from Sinopharm Chemical Reagent Co., Ltd, while 1,2-butanediol (AR, 98%) and glycerol (AR, 99.5%) were supplied by Macklin Biochemical Co., Ltd. All reagents were used without further purification, and deionized water was employed throughout the experiments.

2.2 Catalyst synthesis

In this study, SAPO-11 was employed as the support to prepare a series of Ni–WO_x/SAPO-11 catalysts with varying Ni and W loadings. The synthesis procedure is as follows: first, SAPO-11 powder was calcined at 500 °C to remove potential organic residues. Subsequently, nickel nitrate, ammonium tungstate, and the pretreated SAPO-11 powder (1 g) were co-dispersed in 20 mL of aqueous solution. The Ni and W loadings were adjusted to 10 wt% and 20 wt% (relative to SAPO-11), respectively, followed by 24-hour stirring at room temperature. The mixture was then evaporated in an oil bath at 80 °C and dried completely in an oven for 12 h. After grinding, the precursor was transferred to a tubular furnace and purged under nitrogen flow (100 mL min^{-1}) for 10 minutes, followed by calcination at 500 °C (heating rate: 5 °C min^{-1}) for 3 h. The calcined sample was cooled rapidly and subjected to reduction in a 10% H_2/Ar atmosphere at varying temperatures (heating rate: 5 °C min^{-1}) for 3 h. Finally, the obtained catalysts were sealed and stored in a desiccator. (Additional catalysts with different metal precursors or supports were prepared using analogous protocols.)

2.3 Product analysis

The cellulose hydrogenolysis experiments in this work were conducted in a 50 mL stainless steel autoclave (Model YZPR-50H, Shanghai Yanzheng Experimental Instrument Co., Ltd). The procedure is as follows: cellulose (0.2 g), catalyst (0.1 g), and 20 mL deionized water were loaded into the autoclave. After sealing, hydrogen was purged five times to eliminate air, followed by pressurization with 4 MPa H_2. The reactor was heated to 240 °C at 5 °C min^{-1} and maintained for 4 hours under continuous stirring at 800 rpm. After cooling to room temperature, solid–liquid products were separated *via* filtration, and liquid products were analyzed using high-performance liquid chromatography (Arc HPLC, Waters). The cellulose conversion rate (C-mol%), product yield (C-mol%), and product selectivity (%) in the hydrogenolysis reaction were all calculated based on carbon molar balance. The cellulose conversion rate was determined using eqn (1) and (2).

$$\text{Conv.} = (B_{\text{cellulose}} - A_{\text{cellulose}})/B_{\text{cellulose}} \quad (1)$$

$$A_{\text{cellulose}} = m_{\text{r}} - m_{\text{catalyst}} \quad (2)$$

The yield of hydrogenolysis products was calculated using eqn (3).

$$\text{Yield (C-mol\%)} = (n_i \times k_i \times M_{(C_6H_{10}O_5)})/(6 \times B_{\text{cellulose}}) \quad (3)$$

Here, $B_{\text{cellulose}}$ represents the initial mass of cellulose; $A_{\text{cellulose}}$ is the residual cellulose mass after the reaction; m_r denotes the mass of solid residue after the reaction; m_{catalyst} is the mass of catalyst used in the reaction; n_i refers to the molar quantity of product i; k_i indicates the number of carbon atoms in product i; and $M_{(C_6H_{10}O_5)}$ is the molecular weight of the cellulose structural unit.

2.4 Catalyst characterization

The performance of heterogeneous catalysts is generally limited by two aspects: one related to their structural characteristics, and the other closely associated with the metallic phase. To draw comprehensive conclusions, this work systematically characterized both aspects as described below: for the structural characteristics of the catalysts, the surface morphology was observed using an Inspect F50 scanning electron microscope (SEM, FEI) equipped with EDX spectroscopy. Further analysis of the size and lattice of surface metal particles was conducted *via* high-resolution transmission electron microscopy (HRTEM, JEM 2100F, JEOL). To measure physical properties such as specific surface area, pore volume, pore size, and distribution, samples were first degassed at 150 °C for pretreatment, followed by nitrogen physisorption experiments at −196 °C using an ASAP 2460 surface area analyzer (Micromeritics, USA). For the metallic phase analysis, powder X-ray diffraction (XRD) measurements were performed on a Rigaku SmartLab diffractometer with Cu-Kα radiation to characterize the catalyst composition and crystal structure, with a scanning range of 5°–80° and a scan rate of 5° min^{-1}. X-ray photoelectron spectroscopy (XPS) was carried out on a Thermo Fisher Scientific K-Alpha spectrometer to analyze surface elemental composition and chemical states, using Al-Kα radiation (photon energy $h\nu$ = 1486.68 eV) and calibrating binding energies against the C 1s peak at 284.8 eV. Hydrogen temperature-programmed reduction (H_2-TPR) tests were conducted to determine the reduction temperatures of metal elements in the catalyst. Samples were first treated under argon flow (Ar, 99.999%) at 300 °C for 1 hour, cooled to 45 °C, and then exposed to a 10% H_2/Ar mixture while heating to 800 °C at 5 °C min^{-1}.

Additionally, surface acidity was analyzed through NH_3-TPD and pyridine-adsorption infrared spectroscopy (Py-IR) as follows: (1) ammonia temperature-programmed desorption (NH_3-TPD) was performed to determine the acid strength and acid quantity of the catalyst. The sample was first placed in a helium flow (50 mL min^{-1}) and purged at 300 °C for 1 h, then cooled to 50 °C. Subsequently, a 10% NH_3/He gas mixture was introduced until adsorption saturation. The gas flow was then switched back to pure helium (50 mL min^{-1}) for 1 h to remove physisorbed NH_3. Finally, the temperature was increased to 800 °C at a heating rate of 10 °C min^{-1}. The gas consumption during this process was monitored using a thermal conductivity detector (TCD). (2) Pyridine-adsorption Fourier-transform infrared spectroscopy (Py-IR) was conducted on a Bruker Tensor-27 spectrometer to analyze the types of acid sites on the catalyst surface. The sample was pretreated under vacuum at 400 °C for 1 h and cooled to room temperature. Pyridine vapor was introduced into the *in situ* cell and equilibrated for 30 min. The temperature was then raised to 150 °C and 350 °C, and spectral signals in the 1400–1700 cm^{-1} wavenumber range were scanned and collected.

3. Result and discussion

We screened solid acid supports with varying pore sizes and metal types for cellulose hydrogenolysis, and the results are summarized in Table 1. It can be observed that Ni–WO_x/SAPO-11 exhibits excellent selectivity toward ethylene glycol (EG), achieving a carbon molar yield of 49.5% for EG. For comparison, pure SAPO-11 (Entry 8) was tested under identical conditions, revealing incomplete cellulose conversion and negligible EG selectivity. This clearly demonstrates that an acidic support alone cannot effectively drive cellulose hydrolysis in the absence of metallic active sites. In the case of Ni/SAPO-11 (Entry 5), the

Table 1 Evaluation of different catalysts

			Yield[c]/C-mol (%)						
Entry	Catalyst	Conv.[b] (%)	EG	Sor	1,2-PG	1,2-BDO	Gly	Glu	Others
1	Ni–WO_x/HY	43.5	15.1	2.3	3.5	2.1	0.3	4.8	3.6
2	Pt–WO_x/HY[a]	50.3	21.3	3.1	2.2	0.5	0.5	4.1	5.2
3	Pt–WO_x/ZSM5[a]	55.6	14.9	10.1	5.3	1.2	1.2	3.5	5.5
4	Ni–WO_x/ZSM5	50.9	—	20.1	2.5	5.6	0.6	2.1	4.9
5	Ni/SAPO-11	65.2	5.1	35.5	8.3	1.1	0.7	5.5	2.5
6	Ni–WO_x/SAPO-11	88.9	49.5	3.1	6.5	1.2	2.1	0.6	7.8
7	Pt–WO_x/SAPO-11[a]	27.2	5.0	0.1	0.5	0.2	1.2	5.5	4.1
8	SAPO-11	20.3	—	2.1	—	—	0.2	5.1	4.8

[a] Experimental conditions: 0.2 g cellulose, 0.1 g catalyst, 20 mL deionized water, 220 °C, 3 MPa H_2, 4 h, and 800 rpm. Pt loading is 1 wt%. [b] The conversion (wt%) was calculated by the weight of cellulose before and after reaction. [c] Abbreviations: EG (ethylene glycol), Sor (sorbitol), 1,2-PG (1,2-propanediol), 1,2-BDO (1,2-butanediol), Glu (glucose), Gly (glycerol), others (include methanol, *n*-propanol). The remaining carbon balance can be attributed to the humins and gaseous products.

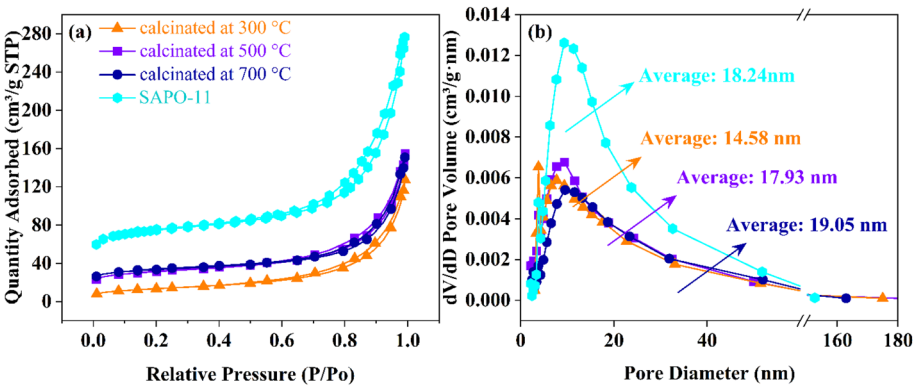

Fig. 1 N_2 adsorption–desorption isotherms (a) and pore size distribution (b) of Ni–WO_x/SAPO-11 catalysts at different reduction temperatures.

total selectivity toward diols (EG, 1,2-PG, 1,2-BDO) was 14.5%, while sorbitol yield reached 35.5%. This indicates that monometallic Ni lacks the ability to cleave C–C bonds, resulting in limited low-carbon product formation. Most glucose intermediates underwent direct hydrogenation on Ni sites to form sorbitol rather than undergoing C–C bond scission.

3.1 Catalyst characterization

3.1.1 Morphological and structural analysis. To explain the catalytic behavior, we conducted systematic characterization of the Ni–WO_x/SAPO-11 catalyst series. The nitrogen adsorption/desorption curves and related data of different catalysts are shown in Fig. 1a and Table S1.† The Ni–WO_x/SAPO-11 catalyst exhibits Type IV nitrogen adsorption/desorption isotherms. A sharp increase in adsorption capacity is observed at relative pressures (P/P_0) of 0.8–1.0, accompanied by a small H3-type hysteresis loop, indicating the presence of mesoporous structures.[16,17] These mesopores facilitate oligosaccharide transport and enhance interactions between intermediate and acid sites.[14] At low relative pressures (P/P_0 < 0.05), the lower adsorption values suggest the coexistence of microporous zeolitic frameworks.[18] The specific surface area of the catalyst exhibited a progressive increase from 48.5 $m^2\ g^{-1}$ (300 °C) to 123.4 $m^2\ g^{-1}$ (700 °C) with elevated reduction temperatures. This enhancement is likely attributed to strengthened metal–metal and metal–support interactions under high-temperature conditions, which mitigate pore blockage and promote hierarchical porosity formation.[19] Furthermore, pore size distribution analysis (Fig. 1b) revealed a significant reduction in 4–5 nm pore volume with increasing reduction temperatures, suggesting partial pore blockage by W particles migrating into mesopores during high-temperature treatment. Compared to pristine SAPO-11, the metal-loaded catalysts demonstrated reduced specific surface area and total pore volume, which can be attributed to partial pore occupation by Ni and W species during impregnation and subsequent thermal treatments.

The morphology and structure of the catalyst were further analyzed using scanning electron microscopy (SEM) and

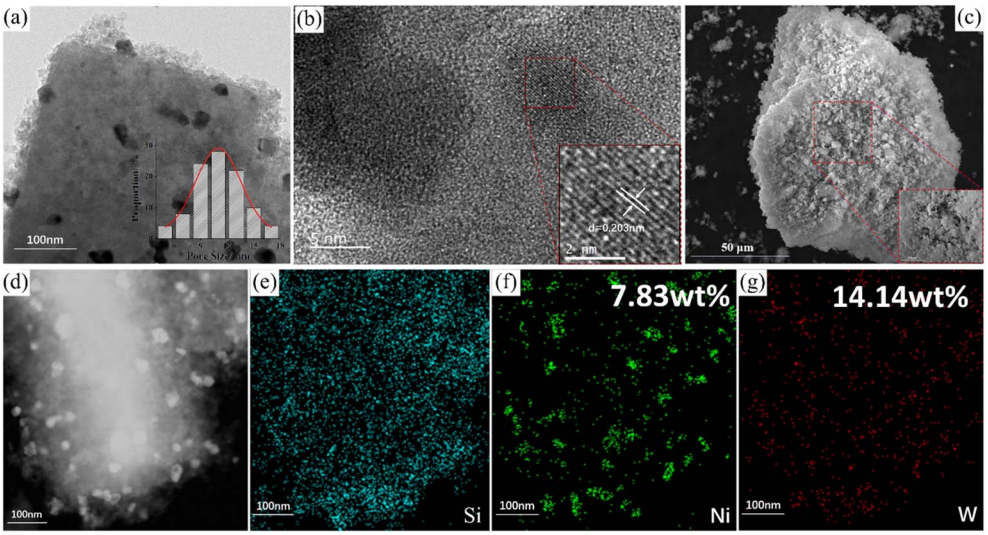

Fig. 2 Morphological characterization and elemental distribution of Ni–WO_x/SAPO-11. (a and b) TEM images; (c) SEM image; (d) HADDF-TEM image; (e–g) EDS mapping.

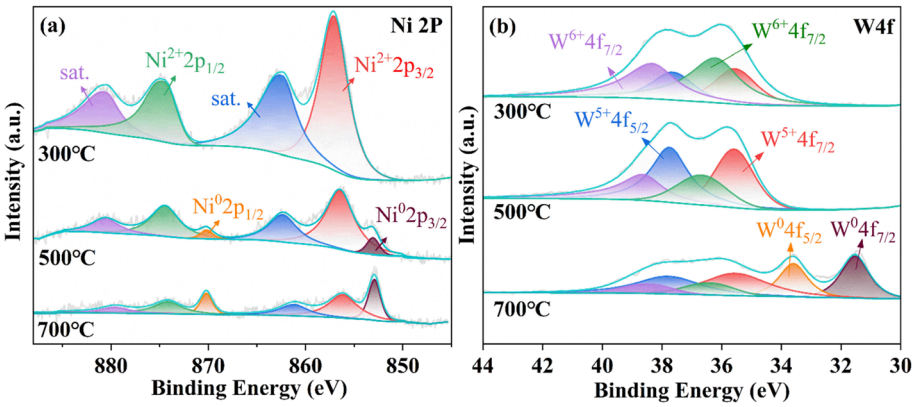

Fig. 3 Ni 2p (a) and W 4f (b) spectra of Ni–WO_x/SAPO-11 catalysts at different reduction temperatures.

transmission electron microscopy (TEM), as shown in Fig. 2. The Ni–WO_x/SAPO-11 catalyst consists of lamellar microcrystals with particle sizes of approximately 2–3 μm.[20] Metallic particles exhibit an average diameter of ~11 nm, with W species (14.14 wt%) uniformly dispersed on the catalyst surface, while Ni species (7.83 wt%) exhibited minor aggregation around W active sites (Table S5†). In Fig. 2b, lattice fringes with a spacing of 0.203 nm are identified, corresponding to the (111) crystallographic plane of metallic Ni^0. Additionally, a significant portion of the observed particles exhibit predominantly amorphous or poorly crystalline characteristics, likely attributed to the presence of amorphous WO_x species.

3.1.2 Metal crystalline phase and valence state analysis. To investigate the chemical states of Ni and W in Ni–WO_x/SAPO-11, high-resolution XPS spectra of Ni 2p and W 4f were analyzed to evaluate the effect of H_2 reduction temperature on metal valences, as shown in Fig. 3a. The Ni 2p spectrum exhibits multiple peaks in the binding energy range of 850–890 eV, including contributions from Ni^0, Ni^{2+}, and their satellite peaks. Specifically, peaks at 852.2 eV and 855.5 eV correspond to Ni^0 and Ni^{2+},[21,22] respectively, while the satellite peak appears at 861.9 eV.[23] With increasing reduction temperature, the peak area ratio of Ni^{2+}/Ni^0 in the catalyst decreases, indicating the progressive reduction of nickel species to their metallic state. In the W 4f spectrum, the peaks at 37.7 eV and 35.6 eV are attributed to the 4f 5/2 and 4f 7/2 orbitals of W^{5+}, while the peaks at 38.6 eV and 36.6 eV correspond to the 4f 5/2 and 4f 7/2 orbitals of W^{6+}.[24,25] The characteristic peaks of W^{5+} and W^{6+} are more pronounced at lower reduction temperatures. As the reduction temperature increases, the ratio of W^{5+}/W^{6+} gradually increases, and almost all of W are converted to metallic W^0 at 700 °C. Notably, the normalized peak intensities demonstrate that the ratio of characteristic peaks attributed to Ni and W to the total spectral area at 700 °C decreases compared to other reduction temperatures (Ni: ~2.8 → 2.10; W: ~6.0 → 1.06, Table S2†), which is likely attributed to the enhanced encapsulation effect of SAPO-11 under high-temperature.[26] Despite this, the EG yield increases at 700 °C. This implies that, instead of the absolute W^{5+} content, the W^{5+}/W^{6+} ratio plays a critical role in C–C cleavage and EG production, which is consistent with prior reports.[27] Additionally, metallic W^0 may partially substitute W^{5+} in facilitating C–C bond cleavage, and it can also form H_xWO_3 in high-temperature water environments to increase Brønsted acidity and alter product selectivity.[28] Nevertheless, the high energy cost associated with achieving W^0 limit its practical applicability.

The XRD patterns of various Ni–WO_x/SAPO-11 catalysts are shown in Fig. 4, including those with different metal ratios (Fig. 4a) and reduction temperatures (Fig. 4b). All catalysts exhibit peaks at 2θ = 8.2, 9.5, 13.2, 15.7, 20.4, 21.0 and 22.2–

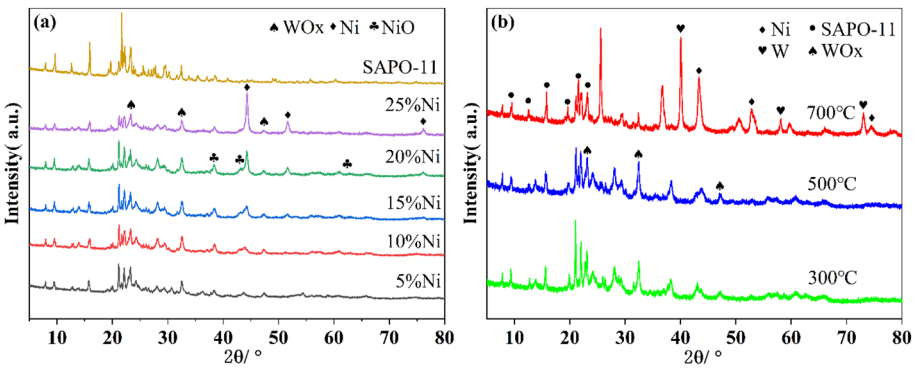

Fig. 4 XRD patterns: (a) Ni–WO_x/SAPO-11 with different Ni ratios; (b) Ni–WO_x/SAPO-11 at different reduction temperatures.

23.6°, which are characteristic of the SAPO-11 molecular sieve with AEL topology (PDF#42-0428), confirming that the framework structure of the support remains intact during catalyst preparation.[17] Notably, the sample reduced at 700 °C shows additional diffraction peaks at 23.5°, 32.7° and 48.1°, corresponding to the (010), (403), and (020) planes of $WO_{2.9}$ (PDF#36-0102).[21] These peaks show slight shifts compared to pure WO_3, which can be attributed to altered W–O bonding energies resulting from strong electronic interactions between Ni and W species.[29] With increasing Ni loading, the diffraction peaks of metallic Ni at 44.6°, 52.0°, and 76.6° intensify significantly. However, the characteristic peaks of NiO at 37.2°, 43.3°, and 62.8° remain unchanged, inferring that excessive Ni loading may alter hydrogenation kinetics and product selectivity. In Fig. 4b, the sample reduced at 700 °C exhibits distinct diffraction peaks at 40.3°, 58.3°, and 73.2°, which are indexed to the (110), (200), and (211) crystallographic planes of metallic tungsten (W^0, PDF#04-0806). This finding is consistent with the metal valence state exhibited in XPS.

H_2-TPR was performed to investigate the reducibility of the catalysts and the interactions between metals and their oxides, as shown in Fig. 5. For catalysts reduced at different temperatures, distinct trends are observed in the TPR profiles. A reduction peak starting at approximately 300 °C corresponds to the reduction of free NiO species, indicating that higher reduction temperatures promote stronger interactions between Ni species and the support.[29] Additionally, the reduction peak near 600 °C is attributed to the reduction of WO_3 to WO_x, while the peak at 705 °C corresponds to the further reduction of WO_x to WO_2. Notably, the H_2 consumption from the calcined precursor to the catalyst reduced at 700 °C correlates with the valence states of Ni and W species observed in XPS (Table S3†). The reduction peaks for W species appear at slightly lower temperatures compared to those reported in literature,[30,31] which is attributed to the interaction between the Ni and W species. The presence of Ni facilitates the reduction of WO_3,[32,33] underscoring the synergistic effects in the Ni–WO_x/SAPO-11 catalytic system.

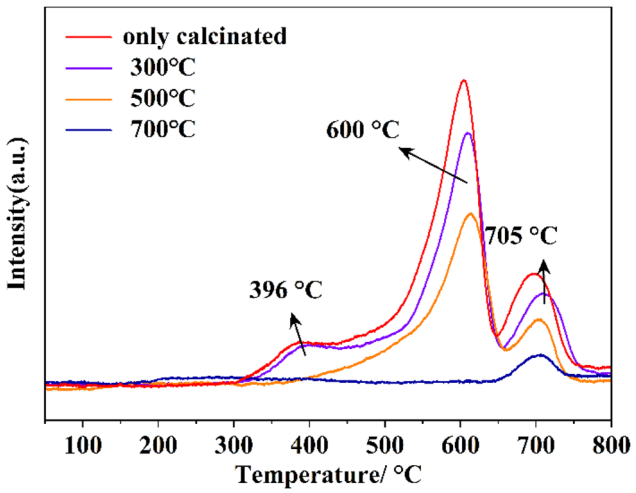

Fig. 5 H_2-TPR profiles of Ni–WO_x/SAPO-11 catalysts at different reduction temperatures.

3.1.3 Effects of the acidic properties. The acidity profiles of Ni–WO_x/SAPO-11 catalysts, including acid strength, acid site density, and acid type distribution, were systematically characterized using ammonia temperature-programmed desorption (NH_3-TPD) and pyridine-adsorption infrared spectroscopy (Py-IR). As illustrated in Fig. 6(a and b), the characteristic absorption bands near 1540 cm^{-1} and 1450 cm^{-1} correspond to pyridine chemically adsorbed on Brønsted (B) and Lewis (L) acid sites, respectively.[10,28] When the desorption temperature was increased from 150 °C to 350 °C, all samples exhibited a decreasing trend in peak intensity and a reduction in total acidity, indicating that the acid sites in the samples were mainly composed by weak acidity (Table S4†).[21] For pure SAPO-11 molecular sieves, the Brønsted acid strength is greater than the Lewis acid strength,[19] and even after metal incorporation, this B/L acid peak intensity ratio remains largely unchanged, underscoring the structural stability of the SAPO-11 framework. Remarkably, the 500 °C-reduced Ni–WO_x/SAPO-11 catalyst demonstrates the highest acid site density (0.13 $mmol_{desorbed\ CO_2}$) and optimal B/L ratio (1.22), attributable to the maximal formation of W^{5+} species. These W^{5+} sites, through their partial hydrolysis to H_xWO_3 clusters, serve as additional Brønsted acid centers, thereby enhancing hydrogenolysis activity.[34] In contrast, reduction at 700 °C induces the conversion of W^{5+} to metallic W^0, resulting in significant loss of acid sites and partial degradation of the support's intrinsic acidity. The results of NH_3-TPD are shown in Fig. 6c, where all catalysts exhibit desorption peaks below 200 °C, reflecting their dominance of weak acid sites.[35] Quantitative analysis of normalized peak areas

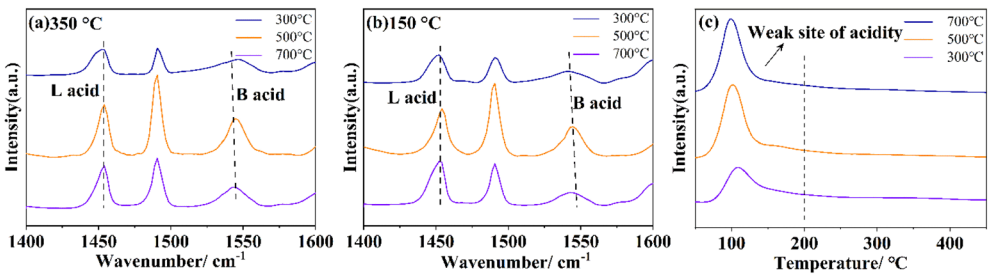

Fig. 6 Acidity analysis of Ni–WO_x/SAPO-11 at different reduction temperatures: (a) Py-FTIR spectra at 350 °C desorption temperature; (b) Py-FTIR spectra at 150 °C desorption temperature; (c) NH_3-TPD profiles.

confirms that the 500 °C-reduced catalyst achieves the highest acid site density (0.13 $mmol_{desorbed\ CO_2}$), followed by 0.11 mmol (700 °C) and 0.09 mmol (300 °C). These trends align precisely with Py-IR data and are rationalized by the evolution of W valence state under different reduction conditions. Overall, the W^{5+}/W^{6+} ratio is a key parameter for controlling the acidity of catalysts. Accurately controlling the W valence state during catalyst synthesis is crucial for adjusting the acidity distribution and hydrogenolysis performance.

3.2 Catalytic performance evaluation

The results of cellulose conversion over catalyst samples prepared under various conditions are presented in Fig. 7 and 8. Fig. 7a illustrates the catalytic performance of Ni–WO_x/SAPO-11 catalysts with varying Ni contents, aiming to identify the optimal Ni loading for cellulose hydrogenolysis. The ICP results of various samples are listed in Table S5.† Under identical reaction conditions, catalysts with Ni loadings ≥10 wt% achieved nearly complete cellulose conversion after 4 hours of reaction. The 10% Ni–20% WO_x/SAPO-11 catalyst demonstrated superior selectivity towards EG, reaching 66.6% selectivity with a total diol selectivity of 75.5%. Notably, the EG yield displayed a volcano-shaped profile with Ni loadings ranging from 5 to 25 wt%. When Ni loading decreased from 25% to 10%, the selectivity toward low-carbon alcohols (EG and 1,2-PG) gradually increased, while sorbitol selectivity declined. This trend implies that elevated Ni loading promotes glucose hydrogenation to sorbitol while suppressing its isomerization to fructose, thereby reducing EG selectivity due to competing pathways for fructose C–C cleavage toward 1,2-PG. However, the overall yield variation remained minor, indicating that EG selectivity is not highly sensitive to Ni content within this range. At 5% Ni loading, the total alcohol selectivity is drastically reduced due to an insufficient number of hydrogenation sites (Table S5†). Collectively, these findings highlight that EG yield critically depends on the synergistic interplay between metal composition and their cooperative catalytic functions.

Subsequently, the influence of catalyst preparation methods on hydrogenolysis performance was investigated, as shown in Fig. 7b. The results reveal that the EG yield over Ni–WO_x/SAPO-11 catalysts calcined at different temperatures under inert atmosphere first increased and then decreased, exhibiting an inverse trend to the 1,2-PG yield. This suggests that excessively high or low calcination temperatures suppress W active sites, impairing C–C cleavage capability and leading to hydrogenation of cellulose intermediates into sorbitol or isomerization-derived byproducts. Additionally, overly high calcination temperatures may induce nickel agglomeration, further reducing EG yields.[14,25] Within the studied range, calcination at 500 °C optimally preserved W site activity, delivering the highest EG yield, thereby demonstrating that adjusting calcination temperature effectively modulates product selectivity. Furthermore, Fig. 7c illustrates the impact of H_2 reduction temperature during catalyst preparation: (1) at 300 °C, incomplete reduction of WO_x resulted in weakened Brønsted acidity and a low total acid amount (0.09 $mmol_{desorbed\ CO_2}$), leading to diminished cellulose conversion and the promotion of humins and

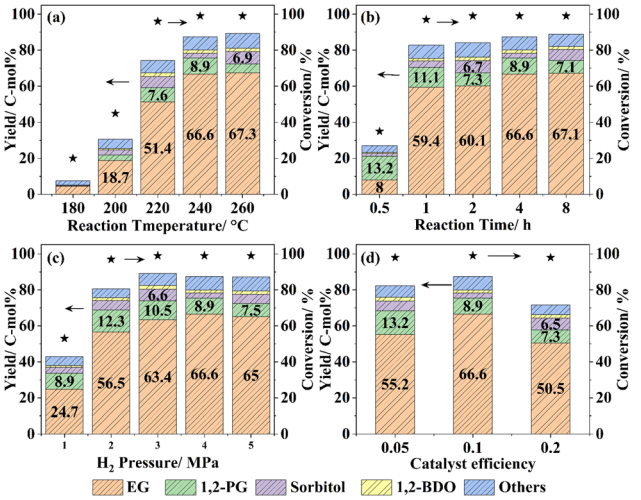

Fig. 8 (a) Reaction temperature; (b) reaction time; (c) hydrogen pressure; (d) catalyst efficiency on the conversion rate of cellulose hydrogenolysis and product selectivity over Ni–WO_x/SAPO-11 ("others" includes 1,2-butanediol, glucose, glycerol, methanol, *n*-propanol. The remaining carbon balance can be attributed to the humins and gaseous products. Experimental conditions: 0.2 g cellulose, 0.1 g catalyst, 20 mL deionized water, 240 °C, 4 MPa H_2, 4 h, and 800 rpm).

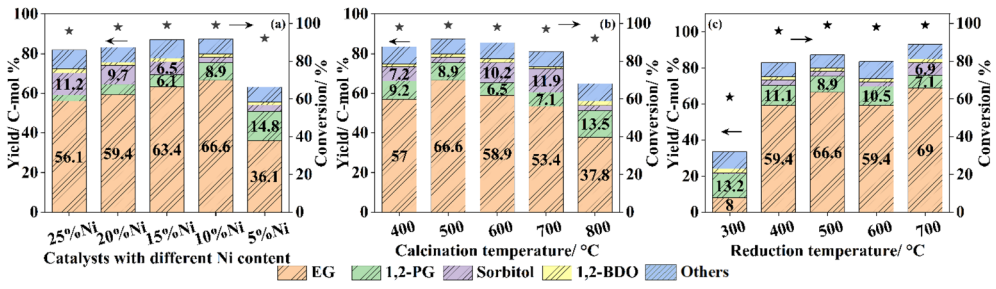

Fig. 7 (a) Metal component ratio; (b) N_2 calcination temperature; (c) H_2 reduction temperature on the conversion rate of cellulose hydrogenolysis and product selectivity over Ni–WO_x/SAPO-11 ("others" includes 1,2-butanediol, glucose, glycerol, methanol, *n*-propanol. The remaining carbon balance can be attributed to the humins and gaseous products. Experimental conditions: 0.2 g cellulose, 0.1 g catalyst, 20 mL deionized water, 240 °C, 4 MPa H_2, 4 h, and 800 rpm).

oligomers formation. (2) At 400–500 °C, the EG yields correlated with a progressive increase in the W^{5+}/W^{6+} ratio, which peaked at 500 °C. This elevated ratio enhanced Brønsted acid strength and promoted C–C cleavage, thereby improving EG selectivity, consistent with prior reports.[27,34] (3)At 700 °C, XPS results confirmed that both metals predominantly existed in metallic states (Ni^0 and W^0). The unexpected rise in EG yield suggests that metallic W^0 could partially substitute W^{5+}/W^{6+} in facilitating hydrogenolysis. Despite the catalyst achieving the highest EG selectivity at 700 °C, the H_2-TPR profiles (Fig. 5a and Table S3†) reveal that the H_2 consumption is significantly higher compared to that under 500 °C. Additionally, the elevated temperature posed safety risks, and the EG selectivity difference between 700 °C and 500 °C was insignificant (66.6% *vs.* 69%). Therefore, 500 °C was selected as the optimal reduction temperature for subsequent reaction optimization.

Next, reaction conditions for cellulose hydrogenolysis were optimized. The effect of temperature on EG production is shown in Fig. 8a. Within the 180–240 °C range, EG yield increased dramatically from 4.4% to 65.6%, indicating that H^+ ions generated in high-temperature aqueous environments significantly promote cellulose hydrolysis.[10] When the temperature was further increased, the EG yield remained relatively stable. Meanwhile, the yields of byproducts such as sorbitol and 1,2-PG showed minor changes, suggesting that EG is more sensitive to reaction temperature. Notably, total carbon recovery in liquid products decreased at elevated temperatures, likely due to thermal degradation into gaseous carbon-containing species. Fig. 8b illustrates the impact of reaction time. At 0.5 h, incomplete cellulose conversion resulted in low yields and selectivity. When the reaction time was extended beyond 1 hour, cellulose could be completely converted. However, as time progressed, the EG yield increased only slightly, indicating that the change in EG yield is relatively gradual compared to the effect of reaction temperature. H_2 pressure effects are shown in Fig. 8c. At 1 MPa, insufficient hydrogen supplies limited reaction progress. Complete conversion was achieved at 2–5 MPa, with EG yield displaying a volcano-shaped trend peaking at 4 MPa. Concurrently, 1,2-PG yield decreased markedly, consisting of competitive pathways between EG and 1,2-PG formation. These findings collectively highlight temperature as the most critical parameter for EG production.

Additionally, the effect of catalyst loading on cellulose hydrogenolysis was investigated, as shown in Fig. 8d. A clear trend is observed: the yields of low-carbon alcohols and EG initially rise and then decline with increasing catalyst dosage. When 50 mg of catalyst was used, insufficient catalyst loading and slow reaction rates hindered timely cleavage of hydrolyzed cellulose intermediates into glycolaldehyde, leading to side reactions such as increased sorbitol formation. Conversely, excessive catalyst (200 mg) introduced abundant active sites that promoted undesirable side reactions, including over-hydrogenation or excessive cracking of reactants/intermediates, thereby reducing EG selectivity. This demonstrates that optimizing catalyst dosage is essential to balance reaction efficiency and product selectivity.

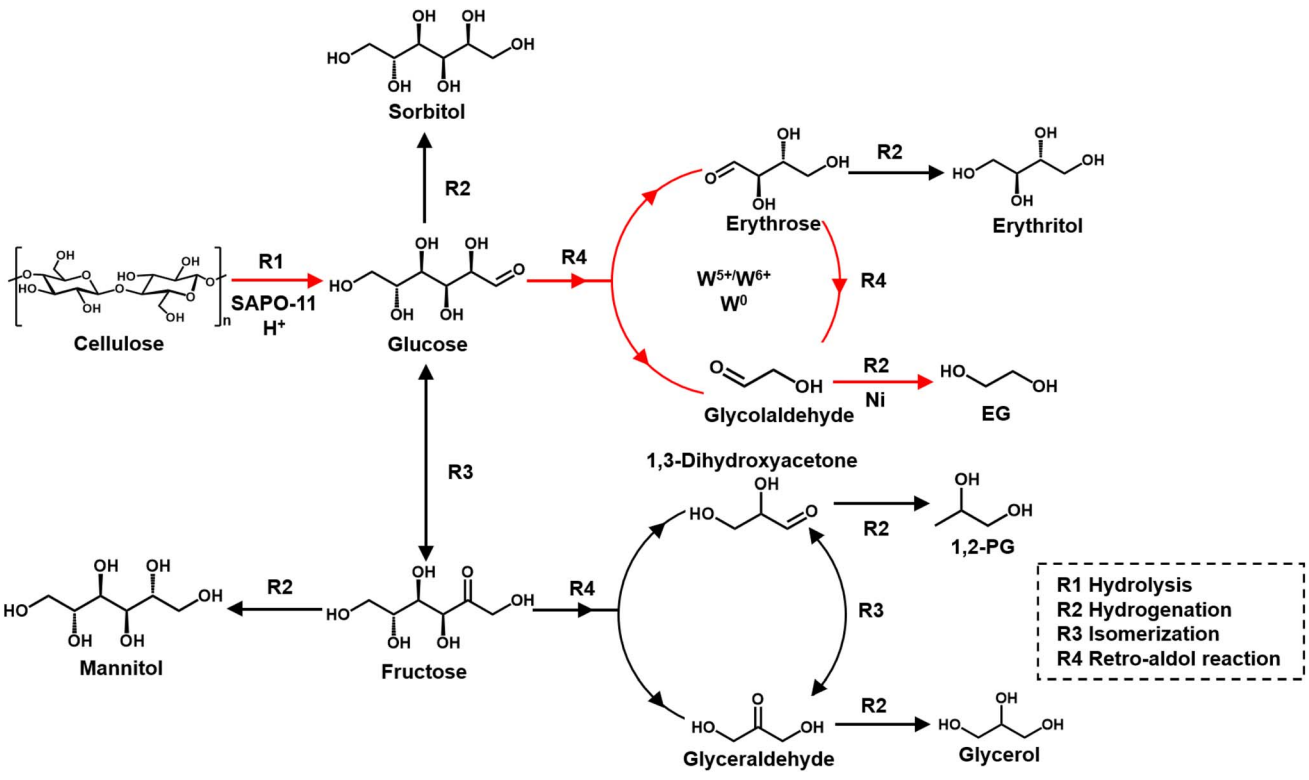

Scheme 1 The reaction pathway of Ni–WO_x/SAPO-11 catalyzing the conversion of cellulose to ethylene glycol.

3.3 Hydrogenolysis path of cellulose based on Ni–WO_x/SAPO-11

The reaction pathway for cellulose hydrogenolysis over the Ni–WO_x/SAPO-11 catalyst is illustrated in Scheme 1. The conversion of cellulose to ethylene glycol (EG) primarily involves three key steps: cellulose is first hydrolyzed to glucose under the combined action of H^+ ions generated from high-temperature water dissociation, moderate acid sites on SAPO-11, and H_xWO_3 species formed *via* dissolution of W^{5+} ions in the aqueous phase.[28] These factors cooperatively cleave the β-1,4-glycosidic bonds in cellulose. Glucose then undergoes C–C bond cleavage *via* retro-aldol condensation catalyzed by W species, yielding glycolaldehyde intermediates. Finally, glycolaldehyde is selectively hydrogenated to EG on Ni^0 metal sites.[36,37] Concurrently, competing side reactions reduce EG selectivity: direct hydrogenation of glucose to sorbitol on Ni sites; isomerization of glucose to fructose, followed by retro-aldol condensation and hydrogenation pathways, generating byproducts such as 1,2-propanediol and glycerol; erythrose (formed *via* glucose C–C cleavage) undergoing hydrogenation to erythritol, which further decomposes into 1,2-butanediol (1,2-BDO) and other byproducts.[14] At 300 °C reduction, the incompletely reduced WO_x fails to efficiently cleave glucose C–C bonds for low-carbon product formation, which allows prolonged residence time, promoting glucose polymerization into humins and consequently reducing EG yield.[37] In contrast, metallic W^0 formed at 700 °C exhibits enhanced C–C cleavage activity, thereby increasing EG yield. These findings underscore that regulating the kinetics of three critical reactions through metal valence state modulation is pivotal for optimizing EG production efficiency. The synergistic coupling of W^{5+}-derived Brønsted acidity and Ni^0-catalyzed hydrogenation enables precise control over reaction selectivity, driving efficient EG formation while minimizing undesired side reactions.

3.4 Catalyst stability

As shown in Fig. 9, the cycling stability of Ni–WO_x/SAPO-11 was investigated. After each hydrogenolysis reaction, the catalyst was recovered by centrifugation, washed with deionized water to neutrality, and freeze-dried for reuse in subsequent cycles. The results indicate that cellulose conversion remained unchanged after five cycles, demonstrating the catalyst's retained activity. However, EG selectivity slightly decreased from 66.6% to 60.9%, with minor reductions in byproduct yields. The observed decline in performance can be attributed to two factors: (1) mass loss during catalyst recovery. (2) Gradual leaching of Ni and W species into the aqueous phase, leading to the loss of active components, consistent with findings reported by Yang *et al.*[12] The relatively stable EG selectivity across cycles suggests that the acid sites provided by SAPO-11 remain robust. Therefore, future research should focus on developing supports that form more stable interactions with metal species to minimize leaching and enhance catalyst recyclability.

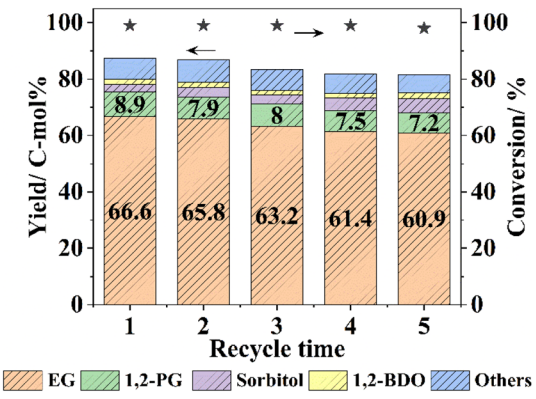

Fig. 9 Cycling test of Ni–WO_x/SAPO-11 catalyst ("others" includes 1,2-butanediol, glucose, glycerol, erythritol, *n*-propanol, *n*-hexanol. The remaining carbon balance can be attributed to the humins and gaseous products. Experimental conditions: 0.2 g cellulose, 0.1 g catalyst, 20 mL deionized water, 240 °C, 4 MPa H_2, 4 h, and 800 rpm).

4. Conclusion

This study reports the rational design of a multifunctional Ni–WO_x/SAPO-11 catalyst for the direct hydrogenation of cellulose to prepare EG. Under optimal conditions (10 wt% Ni, 20 wt% W, 500 °C reduction), the catalyst achieved nearly complete cellulose conversion, with EG selectivity of 66.6% and total diol selectivity of 77.3%. Key mechanistic insights reveal that Brønsted acidity derived from W^{5+} species facilitates β-1,4-glycosidic bond cleavage and retro-aldol condensation of glucose, while Ni^0 sites drive hydrogenation of glycolaldehyde intermediates. The hierarchical pore structure of SAPO-11 ensures efficient mass transport, and its moderate acidity minimizes undesired side reactions. Optimal W^{5+}/W^{6+} ratios (achieved at 500 °C) enhance C–C cleavage through Brønsted acid site formation, metallic W^0 formation at 700 °C introduces alternative pathways for bond scission, albeit with compromised acid site density. These findings provide a reference for the rational design of catalysts for cellulose hydrolysis into small molecule products in the future.

Data availability

Data supporting the findings of this study are available from the corresponding authors upon reasonable request. Correspondence and requests for materials should be addressed to X. Z. Zhuang.

Conflicts of interest

There are no conflicts to declare.

Acknowledgements

This work was supported financially by the National Natural Science Foundation of China (no. 22479024), the National Key R&D Program of China (no. 2022YFB4201804), Jiangsu Funding Program for Excellent Postdoctoral Talent (2023ZB175) and Fundamental Research Funds for the Central Universities (2242022R10058).

References

1 J. X. Xi, D. Q. Ding, Y. Shao, X. H. Liu, G. Z. Lu and Y. Q. Wang, Production of Ethylene Glycol and Its Monoether Derivative from Cellulose, *ACS Sustain. Chem. Eng.*, 2014, **2**(10), 2355–2362.

2 W. P. Deng, Q. H. Zhang and Y. Wang, Catalytic transformation of cellulose and its derived carbohydrates into chemicals involving C-C bond cleavage, *J. Energy Chem.*, 2015, **24**(5), 595–607.

3 L. R. Bao, S. H. Zhu, Y. Chen, Y. Wang, W. H. Meng, S. Xu, Z. H. Lin, X. Y. Li, M. Sun and L. M. Guo, Anionic defects engineering of Co3O4 catalyst for toluene oxidation, *Fuel*, 2022, **314**, 7.

4 N. Ji, T. Zhang, M. Zheng, A. Wang, H. Wang, X. Wang and J. G. Chen, Direct catalytic conversion of cellulose into ethylene glycol using nickel-promoted tungsten carbide catalysts, *Angew Chem. Int. Ed. Engl.*, 2008, **47**(44), 8510–8513.

5 N. Mosier, C. Wyman, B. Dale, R. Elander, Y. Y. Lee, M. Holtzapple and M. Ladisch, Features of promising technologies for pretreatment of lignocellulosic biomass, *Bioresour. Technol.*, 2005, **96**(6), 673–686.

6 S. B. Liu, M. Tamura, Y. Nakagawa and K. Tomishige, One-Pot Conversion of Cellulose into n-Hexane over the Ir-ReOx/SiO2 Catalyst Combined with HZSM-5, *ACS Sustain. Chem. Eng.*, 2014, **2**(7), 1819–1827.

7 L. Hu, L. Lin, Z. Wu, S. Y. Zhou and S. J. Liu, Chemocatalytic hydrolysis of cellulose into glucose over solid acid catalysts, *Appl. Catal., B*, 2015, **174**, 225–243.

8 A. H. Xin, S. T. Yu, L. Jiang, D. F. Yin, L. Li, C. X. Xie, L. Wu, H. L. Yu, Y. X. Liu, Y. Liu and S. W. Liu, Bifunctional Catalyst with a Yolk-Shell Structure Catalyzes Glucose to Produce Ethylene Glycol, *J. Phys. Chem. C*, 2021, **125**(12), 6632–6642.

9 Y. Weng, Y. Wang, M. Zhang, X. Wang, Q. Sun, S. Mu, H. Wang, M. Fan and Y. Zhang, Selectively chemo-catalytic hydrogenolysis of cellulose to EG and EtOH over porous SiO2 supported tungsten catalysts, *Catal. Today*, 2023, **407**, 89–95.

10 H. Huang, L. Chen, C. Gu, X. Zhang, J. Liu, Q. Zhang, C. Wang, L. Ma and Y. Liao, In-situ synthesis of Ru–WOx/biochar catalyst for conversion of cellulose toward ethylene glycol, *Cellulose*, 2022, **29**(15), 8195–8211.

11 P. H. Yan, X. X. Tian, E. M. Kennedy and M. Stockenhuber, Advanced in situ IR spectroscopy study of anisole hydrodeoxygenation over Ni/SiO2 catalysts, *J. Catal.*, 2023, **427**, 12.

12 X. Yang, Z. Li, M. Guo, T. Zhao, X. Su, W. Jiang, G. Han and H. Ben, Synergistic effects of WO3 and NiCu bimetals for the One-Pot conversion of cellulose into ethylene glycol, *Fuel*, 2023, **341**, 127560.

13 P. H. Yan, I. N. Azreena, H. Peng, H. Rabiee, M. Ahmed, Y. L. Weng, Z. H. Zhu, E. M. Kennedy and M. Stockenhuber, Catalytic hydropyrolysis of biomass using natural zeolite-based catalysts, *Chem. Eng. J.*, 2023, **476**, 13.

14 N. Li, X. Liu, J. Zhou, Q. Ma, M. Liu and W. Chen, Enhanced Ni/W/Ti Catalyst Stability from Ti–O–W Linkage for Effective Conversion of Cellulose into Ethylene Glycol, *ACS Sustain. Chem. Eng.*, 2020, **8**(26), 9650–9659.

15 X. J. Dai, Y. Cheng, T. T. Liu and L. J. Mao, Synthesis, Modification, and Performance Regulation of SAPO-11 Molecular Sieve and Development of n-Alkane Hydroisomerization Catalyst: A Mini-Review, *Energy Fuels*, 2024, **38**(11), 9262–9279.

16 H. S. Xin, H. Y. Wang, X. H. Hu, X. Z. Zhuang, L. Yan, C. G. Wang, L. L. Ma and Q. Y. Liu, Cellulose hydrogenolysis to alcohol and ketone products using Co@C catalysts in the phosphoric acid aqueous solution, *React. Chem. Eng.*, 2022, **8**(1), 64–76.

17 D. J. Zheng, D. L. Guo, Z. X. Wang, X. S. Wang, Y. L. Shan, X. M. Liu, Z. F. Yan, S. T. Yu and Y. X. Liu, Synergistic effect of CoOx and Ni-Co alloy in Ni-Co/SAPO-11 catalysts for the deoxygenation of stearic acids, *Chem. Eng. J.*, 2023, **451**, 8.

18 S. Khan, K. M. Qureshi, A. N. K. Lup, M. F. A. Patah and W. Daud, Role of Ni-Fe/ZSM-5/SAPO-11 bifunctional catalyst on hydrodeoxygenation of palm oil and triolein for alternative jet fuel production, *Biomass Bioenergy*, 2022, **164**, 11.

19 Y. L. Huang, Y. Y. Wang, C. J. Zuo, X. L. Sheng, Y. Z. Huang, Y. W. Zhang and Y. M. Zhou, Pt-Zn Bimetallic Nanoclusters Encapsulated in SAPO-11 Molecular Sieve with Excellent Catalytic Performance for Levulinic Acid Hydrogenation, *Catal. Lett.*, 2023, **153**(9), 2651–2664.

20 X. Li, F. Rezaei and A. A. Rownaghi, Methanol-to-olefin conversion on 3D-printed ZSM-5 monolith catalysts: Effects of metal doping, mesoporosity and acid strength, *Microporous Mesoporous Mater.*, 2019, **276**, 1–12.

21 H. Y. Wang, H. S. Xin, C. L. Cai, C. H. Zhu, Z. X. Xiu, Q. Y. Liu, Y. J. Weng, C. G. Wang, X. H. Zhang, S. J. Liu, Z. F. Peng and L. L. Ma, Selective C3-C4 Keto-Alcohol Production from Cellulose Hydrogenolysis over Ni-WOx/C Catalysts, *ACS Catal.*, 2020, **10**(18), 10646–10660.

22 P. H. Yan, S. B. Xi, H. Peng, D. R. G. Mitchell, L. Harvey, M. Drewery, E. M. Kennedy, Z. H. Zhu, G. Sankar and M. Stockenhuber, Facile and Eco-Friendly Approach To Produce Confined Metal Cluster Catalysts, *J. Am. Chem. Soc.*, 2023, **145**(17), 9718–9728.

23 J. Yu, J. Liang, X. Chen, L. Wang, X. Wei, Y. Qin, Y. Li and Y. Ling, Reaction network and kinetics for the one-pot hydrogenolysis of cellulose to ethylene glycol over NiOx-WOy-Cu/MgAl2O4, *React. Kinet. Mech. Catal.*, 2021, **133**(1), 55–71.

24 X. L. Yang, R. H. Gao, W. L. Dai and K. N. Fan, Influence of tungsten precursors on the structure and catalytic properties of WO3/SBA-15 in the selective oxidation of cyclopentene to glutaraldehyde, *J. Phys. Chem. C*, 2008, **112**(10), 3819–3826.

25 Y. L. Cao, J. W. Wang, M. Q. Kang and Y. L. Zhu, Efficient synthesis of ethylene glycol from cellulose over Ni-WO3/SBA-15 catalysts, *J. Mol. Catal. A: Chem.*, 2014, **381**, 46–53.

26 Y. Wu, C. Dong, H. Wang, J. Peng, Y. Li, C. Samart and M. Ding, One-Pot Ethanol Production from Cellulose

Transformation over Multifunctional Pt/WOx and Hollow Pt@HZSM-5 Catalysts, *ACS Sustain. Chem. Eng.*, 2022, **10**(8), 2802–2810.

27 D. Chu, Y. Xin and C. Zhao, Production of bio-ethanol by consecutive hydrogenolysis of corn-stalk cellulose, *Chin. J. Catal.*, 2021, **42**(5), 844–854.

28 Y. J. Weng, Y. Wang, M. W. Zhang, X. L. Wang, Q. Sun, S. F. Mu, H. Y. Wang, M. H. Fan and Y. L. Zhang, Selectively chemo-catalytic hydrogenolysis of cellulose to EG and EtOH over porous SiO2 supported tungsten catalysts, *Catal. Today*, 2023, **407**, 89–95.

29 E. Soghrati, C. Kok Poh, Y. H. Du, F. Gao, S. Kawi and A. Borgna, C-O Hydrogenolysis of Tetrahydrofurfuryl Alcohol to 1,5-Pentanediol Over Bi-functional Nickel-Tungsten Catalysts, *ChemCatChem*, 2018, **10**(20), 4652–4664.

30 D. C. Vermaire and P. C. Vanberge, The preparation of WO3TiO2 and Wo3Al2O3 and characterization by temperature-programmed reduction, *J. Catal.*, 1989, **116**(2), 309–317.

31 N. X. Li, Y. Zheng, L. F. Wei, H. C. Tenga and J. C. Zhou, Metal nanoparticles supported on WO3 nanosheets for highly selective hydrogenolysis of cellulose to ethylene glycol, *Green Chem.*, 2017, **19**(3), 682–691.

32 K. Fabicovicová, M. Lucas and P. Claus, From microcrystalline cellulose to hard- and softwood-based feedstocks: their hydrogenolysis to polyols over a highly efficient ruthenium-tungsten catalyst, *Green Chem.*, 2015, **17**(5), 3075–3083.

33 Z. F. Huang, J. J. Song, L. Pan, X. W. Zhang, L. Wang and J. J. Zou, Tungsten Oxides for Photocatalysis, Electrochemistry, and Phototherapy, *Adv. Mater.*, 2015, **27**(36), 5309–5327.

34 J. Chai, S. Zhu, Y. Cen, J. Guo, J. Wang and W. Fan, Effect of tungsten surface density of WO3–ZrO2 on its catalytic performance in hydrogenolysis of cellulose to ethylene glycol, *RSC Adv.*, 2017, **7**(14), 8567–8574.

35 P. Ning, Z. X. Song, H. Li, Q. L. Zhang, X. Liu, J. H. Zhang, X. S. Tang and Z. Z. Huang, Selective catalytic reduction of NO with NH3 over CeO2–ZrO2–WO3 catalysts prepared by different methods, *Appl. Surf. Sci.*, 2015, **332**, 130–137.

36 Y. Li, Y. C. Zhang, Z. Y. Li, H. Y. Zhang and P. Fu, Reaction pathways and selectivity in the chemo-catalytic conversion of cellulose and its derivatives to ethylene glycol: A review, *Chin. J. Chem. Eng.*, 2024, **66**, 310–331.

37 X. Z. Zhuang, H. Y. Wang, S. G. Jiang, X. H. Hu, T. Su, X. H. Zhang and L. L. Ma, A review on the chemo-catalytic conversion of cellulose to bio-ethanol, *Green Chem. Eng.*, 2024, **5**(3), 276–289.